Aging-Aware Optimal Energy Management Control for a Parallel Hybrid Vehicle Based on Electrochemical-Degradation Dynamics

Luca De Pascali, Francesco Biral, and Simona Onori, *Senior Member, IEEE*

***Abstract*—Hybrid electric vehicles offer the best alternative to gasoline-only powered vehicles as they combine a conventional propulsion system with an electric propulsion system. A supervisory controller is needed to optimally manage the energy on-board. Published works on this topic have mainly focused on strategies aimed at minimizing the fuel consumption. In this article, we address the problem of designing a supervisory controller that achieves minimum fuel consumption while optimally preserving battery life. Electrochemical degradation dynamics are used in the multi-objective problem formulation to accurately capture, and control battery performance, and aging during the control design phase. The electrochemical degradation model accounts for the electrolyte dynamics to capture high C-rate operation of the battery which are properl in charge sustaining hybrid powertrains. We resort to the optimal control formalism, and nonlinear optimization techniques along with the full discretization approach (in the state, and in the control) to cast the energy management problem into a large scale non-linear programming problem, that is able to deal with multi-scale dynamics, namely from the stiff electrolyte battery dynamics to map-based slow dynamics of the actuators. Numerical simulations conducted over four different standard driving cycles (with, and without road grades) show that our aging-aware energy management approach is able to significantly reduce the deterioration of the battery, while retaining very good fuel reduction performance.**

***Index Terms*—.**

I. Introduction

THE increasing concerns about the reduction of greenhouse gases have moved the joint interest of governments, industries and academia towards the development of a clean and sustainable mobility. Hybrid electric vehicles (HEVs) are blending the transition towards the full-electric mobility, since they run on both electric and petrol power, in a proportion that is dependent on the level of hybridization of the powertrain architecture: from start&stop micro hybrid to plug-in hybrids where the internal combustion engine serves solely as a range extender that supports the main electric motor. All the hybrid electric vehicles have at least two power-sources that contribute in delivering the required power to the wheels.

There is a vast literature on control strategies aimed at the optimization of the fuel economy in HEVs, spanning from heuristic strategies as the thermostatic control logic of [1] and [2], Model Predictive Control methods [3] and [4] to the widely adopted Equivalent Consumption Minimization Strategy (ECMS), found e.g. in [5], [6] and [7], based on the necessary optimality conditions stated by the Pontryagin Minimum Principle (PMP)

Convex optimization methods have been used thanks to the availability of off-the-shelf free efficient solvers that allow to find the global optimal solution in a fairly short computational time. The energy management problem is cast as a convex optimization problem in [8], for an HEV with engine start and gearshift costs based on a combination of deterministic dynamic programming (DP) and convex optimization methods. It is shown that the method yields globally optimal results while returning the solution in much less time than the conventional DP method. In [9], the original non-convex HEV problem is relaxed to become a convex optimization problem and solved as such. Stochastic optimization methods have been also proposed to account for random characteristics of the vehicle speed and drivers behaviors. In [10], an on-board learning algorithm for Markov Chain models was proposed to generate transition probability matrices of power demand. Recently, Reinforcement Learning (RL) methods have gained some traction as they cast the optimal HEV problem into a model-free optimal control. In [11] heuristic planning energy management controller, based on a Dyna agent is proposed for real-time fuel saving in PHEVs. In [12], the same group of researchers proposed an adaptive hierarchical energy management strategy for PHEVs through deep learning and genetic algorithm (GA). A recently published survey on RL-based methods for hybrid vehicles optimization can be found in [13].

The reduction of fuel consumption, and consequently of the cost associated to the vehicle usage, is the main objective of the most common energy management techniques; nevertheless, it is well known that a frequent and severe usage of the battery leads to a fast deterioration of its performances, that results in the replacement of the battery system after few years with increase warranty costs. In [14], ECMS strategy is adapted to the case where battery aging cost is added to the fuel cost. In [15], an experimentally validated battery aging model is exploited to setup a multi objective minimization problem for

Manuscript received March 2, 2020; revised June 28, 2020; accepted August 12, 2020. The review of this article was coordinated by Prof. H. Chaoui. *(Corresponding author: Simona Onori.)*

Luca De Pascali and Francesco Biral are with the Department of Industrial Engineering, University of Trento, 38123 Trento, Italy (e-mail: luca.depascali@uintn.it; francesco.biral@uintn.it).

Simona Onori is with the Department of Energy Resources Engineering, Stanford University, Stanford, CA 94305 USA (e-mail: sonori@stanford.edu).

Digital Object Identifier 10.1109/TVT.2020.3019241

the case of Honda Insight. In [16], a battery health-conscious power management is proposed that minimizes the resistance growth film and fuel consumption. The importance of a mindful management of charging operations in extending battery life is highlighted in [17], while battery internal-temperature control is used in [18] to preserve battery life.

In all of the aforementioned articles, the battery system has been modeled with equivalent circuit models. The simplest equivalent circuit comprises a resistance in series with a voltage generator, and the state-of-charge is the only state; the model is able to capture the static relation between battery current and terminal voltage, but as thoroughly discussed in [19], the model is affected by a large error compared to the models that take voltage dynamics into account.[1] This error is amplified in conditions far from the equilibrium, e.g. for high charge/discharge current values, long-lasting current bursts and at high or low State of Charge (SOC). In [16] an electrochemistry-based battery model for closed-loop verification is used to find the set of admissible controls, yet the optimal control problem is formulated using the simpler equivalent circuit model. As stated in [20], [21], the knowledge of the internal states of the battery given by the first-principle electrochemical battery models is of paramount importance for an accurate description of the aging dynamics.

In this paper, we design an energy management battery health-aware strategy for a parallel HEV based on a reduced order electrochemical model. The accurate knowledge of the internal states of the battery allows to adopt less compelling constraints on the controls and on the battery states; moreover, by reducing the modeling errors with an accurate description of the voltage dynamics, we can better rely on the resulting control strategy.

The paper is organized as follows: in Section II we describe the powertrain model of the parallel HEV considered in this study, by also briefly recalling the main equations of the electrochemical model and of the capacity degradation model. In Section III we state the energy management problem. We show in Section IV, by means of numerical simulation, the results of the optimization method, and finally, in Section V concluding remarks are provided.

II. Development of the Powertrain Model

This research aims at investigating the energy management strategies for a mild parallel hybrid electric passenger car. The powertrain architecture is illustrated in Fig. 1 and comprises of a 8-speed automatic transmission that can be disconnected from the rest of the powertrain by means of a clutch system; the internal combustion engine is assisted by an electric motor that is fed by a low-voltage 48 V battery and is connected to the crankshaft through a reduction ratio.

The electric motor —or Internal Starter Generator (ISG) unit— is always connected to the crankshaft; this simplifies the powertrain but prevents the vehicle from traveling in pure electric mode. The electric motor unit is connected to the engine shaft through the reduction ratio $\gamma_{\mathrm{mot}} > 1$, therefore

[1]The RC-model, that adds a parallel Resistance-Capacitor branch in series to the voltage generator and the resistance, exhibits much better results in [19].

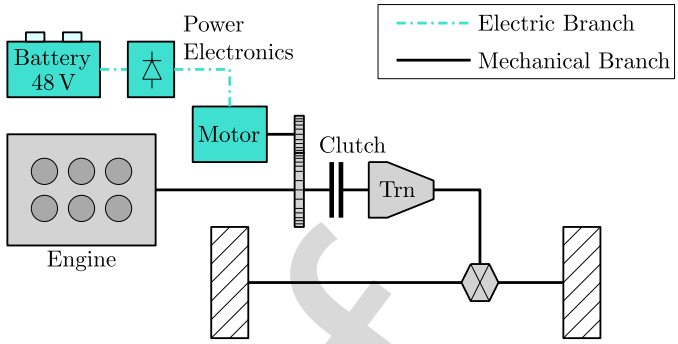

Fig. 1. Architecture of the pre-transmission parallel-hybrid powertrain configuration (P1) under investigation.

TABLE I
Hybrid Vehicle Parameters

Description	Symbol	Value	Unit
Transmission efficiency	η_{trn}	0.95	-
Axle ratio	γ_{axle}	3.730	-
First Gear	$\gamma_{\mathrm{trn},1}$	5.000	-
Second Gear	$\gamma_{\mathrm{trn},2}$	3.200	-
Third Gear	$\gamma_{\mathrm{trn},3}$	2.143	-
Fourth Gear	$\gamma_{\mathrm{trn},4}$	1.720	-
Fifth Gear	$\gamma_{\mathrm{trn},5}$	1.314	-
Sixth Gear	$\gamma_{\mathrm{trn},6}$	1.000	-
Seventh Gear	$\gamma_{\mathrm{trn},7}$	0.822	-
Eighth Gear	$\gamma_{\mathrm{trn},8}$	0.640	-
Motor ratio	γ_{mot}	2.000	-
Vehicle mass	m_{v}	1750	kg
Dyn. wheel radius	r_{w}	0.31	m
Aerodyn. drag coeff.	c_{f}	0.28	$\mathrm{kg\,m^{-1}}$
Rolling resistance coeff	c_{rr0}	0.02	-
Engine inertia	J_{eng}	$2.26 \cdot 10^{-2}$	$\mathrm{kg\,m^2}$
Up-shift engine speed	$\omega_{\mathrm{eng,up}}$	$4.77 \cdot 10^{3}$	rpm
Down-shift engine speed	$\omega_{\mathrm{eng,down}}$	$2.87 \cdot 10^{3}$	rpm

$\omega_{\mathrm{mot}}(t) = \omega_{\mathrm{eng}}(t)\,\gamma_{\mathrm{mot}}$. The engine torque $T_{\mathrm{eng}}(\cdot)$ and the motor torque $T_{\mathrm{mot}}(\cdot)$ sum up at the wheels giving the total torque $T_{\mathrm{w}}(\cdot)$ that is expressed by

$$T_{\mathrm{w}}(t) = (T_{\mathrm{eng}}(t) - J_{\mathrm{eng}}\dot{\omega}_{\mathrm{eng}}(t) + T_{\mathrm{mot}}(t)\gamma_{\mathrm{mot}})\eta_{\mathrm{trn}}^{\mathrm{sign}[a_x(t)]}\gamma_{\mathrm{tot}} + T_{\mathrm{brk}}(t), \quad (1)$$

where $\gamma_{\mathrm{tot}} = \gamma_{\mathrm{trn}}(t)\,\gamma_{\mathrm{axle}}$ is the total transmission ratio, $a_x(\cdot)$ is the vehicle longitudinal acceleration and $T_{\mathrm{brk}}(\cdot)$ is the torque exerted by the mechanical brakes on the wheels. The system parameters are listed in Table I. The term $J_{\mathrm{eng}}\,\dot{\omega}_{\mathrm{eng}}(t)$ represents the extra-torque needed to accelerate the engine. The transmission ratio $\gamma_{\mathrm{trn}}(t) \in \{\gamma_{\mathrm{trn},1}, \ldots, \gamma_{\mathrm{trn},8}\}$ switches among the eight ratios according to the simple speed-based strategy

- if $\omega_{\mathrm{eng}}(t) > \omega_{\mathrm{eng,up}}$, up-shift
- if $\omega_{\mathrm{eng}}(t) < \omega_{\mathrm{eng,down}}$, down-shift

A. Driving Cycle and Longitudinal Dynamics

We formulate the optimization problem by constraining the speed of the vehicle to follow the velocity profile imposed by the driving cycle. We solve the optimization over four driving cycles, with different speed and altitude profiles: the NEDC, the

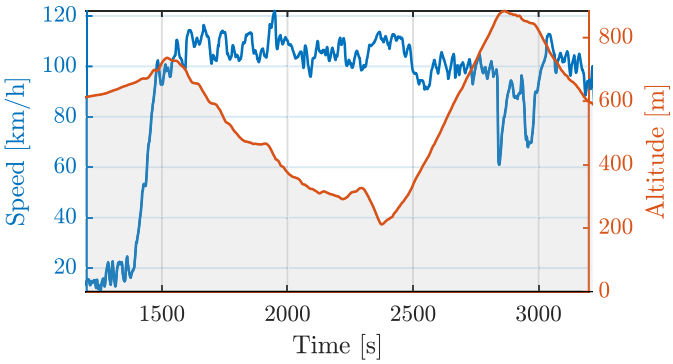

Fig. 2. Vail2NREL mountain driving cycle.

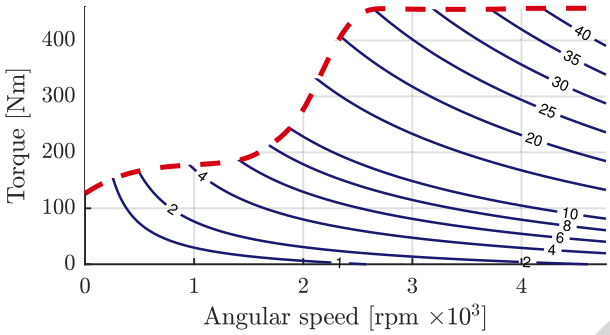

Fig. 3. Engine fuel consumption rate in kg/h (blue solid lines) and torque limits (red dashed lines).

new standard WLTP and the US06 [22] driving cycles are used in emission type-approval tests for passenger cars (the former ones in Europe, the latter mostly in the United States); the last driving cycle, called Vail2NREL in Fig. 2, is a demanding high elevation driving cycle. The torque required at the wheels at time t is computed from the longitudinal dynamics equation

$$T_{\mathrm{w}}(t) = \left(c_{\mathrm{f}}\, v_x(t)^2 + m_{\mathrm{v}}\, a_x(t)\right) r_{\mathrm{w}} + \left(g\, m_{\mathrm{v}}\, (\sin[\sigma(t)] + c_{\mathrm{rr0}} \cos[\sigma(t)]\,)\right) r_{\mathrm{w}}, \quad (2)$$

where $\sigma_{\mathrm{road}}(\cdot)$ is the road slope and $v_x(\cdot)$ is the longitudinal vehicle speed, both taken from the four driving profiles. If we impose the vehicle speed and the road slope according to the selected driving profile, then the torque at wheel $T_{\mathrm{w}}(\cdot)$ is known from (2).

B. Engine

The instantaneous fuel consumption map in Fig. 3 is derived from the engine efficiency and depends on the torque and speed at the motor shaft. The 2D map is well approximated by Willan's lines approach [23], that states that there exists an affine relationship between the fuel consumption rate $\dot{m}_{\mathrm{f}}$ — which is proportional to the power generated by the combustion through the specific calorific value — and the mechanical power output by the engine $P_{\mathrm{eng}}(t) = \omega_{\mathrm{eng}}(t)\, T_{\mathrm{eng}}(t)$. Therefore the instantaneous fuel consumption rate at time t becomes

$$\dot{m}_{\mathrm{f}}(\omega_{\mathrm{eng}}(t), T_{\mathrm{eng}}(t)) = \alpha(\omega_{\mathrm{eng}}(t))\, P_{\mathrm{eng}} + \beta(\omega_{\mathrm{eng}}(t)), \quad (3)$$

TABLE II
WILLAN'S COEFFICIENTS

	$i=1$	$i=2$	$i=3$
α_i	$6.1454 \cdot 10^{-8}$	$-5.2369 \cdot 10^{-11}$	$7.4707 \cdot 10^{-14}$
β_i	$7.0402 \cdot 10^{-6}$	$8.3295 \cdot 10^{-7}$	$6.2962 \cdot 10^{-10}$

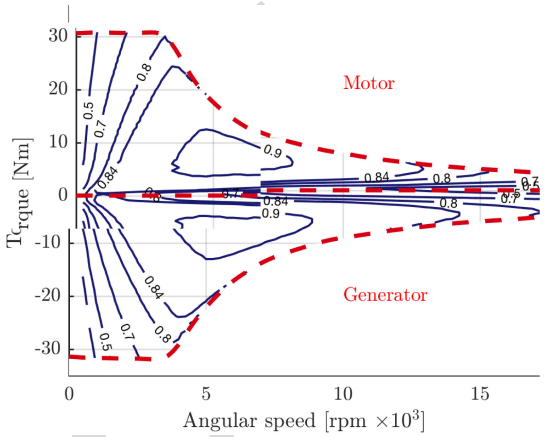

Fig. 4. Motor/generator efficiency contours and torque limits.

with $\alpha(\omega_{\mathrm{eng}}(\cdot)) = \sum_{i=0}^{3} \alpha_i\, \omega_{\mathrm{eng}}^{i-1}(\cdot)$ and $\beta(\omega_{\mathrm{eng}}(\cdot)) = \sum_{i=0}^{3} \beta_i\, \omega_{\mathrm{eng}}^{i-1}(\cdot)$. The Willan's parameters used in this work have been identified for an engine of a SUV class vehicle and are reported in Table II.

C. Motor

The ISG unit of the 48 V hybrid vehicle operates in two working modes: as a *motor* the ISG converts the electrical energy from the battery to mechanical energy at the shaft, while as a *generator* recovers the kinetic energy during a regenerative braking by transforming it to electrical energy that is stored in the battery. The overall power generated (generator mode) or absorbed (motor mode) by the ISG unit is computed considering the non-unitary efficiency $\eta_{\mathrm{mot}}(t)$ that depends on the ISG shaft speed $\omega_{\mathrm{mot}}(\cdot)$ and torque $T_{\mathrm{mot}}(\cdot)$ as

$$P_{\mathrm{mot}}(\cdot) = \begin{cases} \omega_{\mathrm{mot}}(t) T_{\mathrm{mot}}(t) \eta_{\mathrm{mot}}(t) & T_{\mathrm{mot}}(t) < 0, \text{ gen.} \\ \frac{\omega_{\mathrm{mot}}(t) T_{\mathrm{mot}}(t)}{\eta_{\mathrm{mot}}(t)} & T_{\mathrm{mot}}(t) \geq 0, \text{ mot.} \end{cases} \quad (4)$$

where $\eta_{\mathrm{mot}}(\cdot)$ depends on the motor characteristics and is usually represented by iso-efficiency lines as in Fig. 4.

If we approximate the ISG efficiency map with a polynomial surface, we should use high order polynomials that are able to capture the steep slopes close to the efficiency holes at low speed and large torque (and at small torque and high speed); this increases the complexity of the formulation and leads to badly scaled derivatives that could undermine the robustness of the optimization algorithm. To overcome this issue, we propose to directly compute the ISG power for every pair $(\omega_{\mathrm{mot}}, T_{\mathrm{mot}})$ present in the efficiency map; the resulting surface in Fig. 5 is much smoother than the efficiency surface and could be

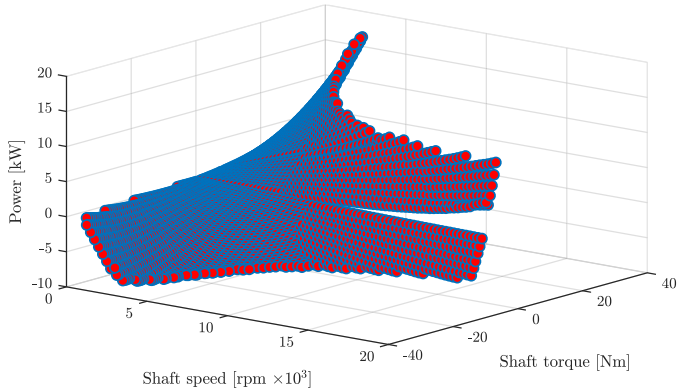

Fig. 5. Actual motor power computed for each element of the efficiency map from (4).

approximated with good accuracy by the third order polynomial

$$P_{\rm mot}(\omega_{\rm mot}(t), T_{\rm mot}(t)) = \sum_{j=0}^{3}\sum_{i=0}^{3} p_{i,j}\,\omega_{\rm mot}(t)^j\,T_{\rm mot}(t)^i. \tag{5}$$

D. Battery System

The Energy Storage System (ESS) comprises of 180 gr/NMC lithium-ion SONY 18650 cylindrical cells arranged in $n_{\rm p} = 16$ parallel modules with $n_{\rm s} = 13$ cells in series.[2] Each cell has a nominal voltage of 3.6 V and nominal capacity equal to 2.0 Ah, resulting in a 48 V battery pack that stores approximately 1.5 kWh of electrical energy in nominal conditions. The maximum discharge/charge power is equal to 17.11 kW and 11.5 kW respectively, corresponding to a maximum cell current equal to 30 A and 20 A respectively. From the battery cell terminal voltage $V(\cdot)$ and the current applied to the cell $I(\cdot)$, the overall battery power at time t is given as:

$$P_{\rm batt}(t) = n_{\rm s}\,n_{\rm p}\,V(t)I(t). \tag{6}$$

Here, we assume that all the cells are balanced and that the battery cooling system is able to keep the cells at a constant temperature uniformly throughout the battery. This is generally not true for standard batteries, in particular for high current values that lead to local temperature gradients; nevertheless, this simplifying assumption is useful to better understand the effect of different temperatures on battery performances and aging, and the analysis can be used to properly size the battery cooling system.

E. Cell Charge/Discharge Dynamics

The Doyle-Fuller-Newman (DFN) electrochemical model describes the diffusion of the lithium ions throughout the cell electrodes and electrolyte [25]. The cell dynamics are described by four coupled nonlinear partial differential equations (PDEs) that represent the transport of charge and mass in the solid and liquid phase. Because of the computational complexity required by the solution of the PDEs, reduced models where capacity and power characteristics of the electrode are lumped into a single particle (Single Particle Model - SPM), are proposed to reduce the dimensionality of the model and make it suitable for control and estimation applications. In this work we use an enhanced version of the SPM (*i.e.* ESPM) that takes the electrolyte dynamics into account to improve the prediction accuracy during high charge/discharge currents ([21], [26]) which are typical of charge-sustaining HEVs.

The model input is the current $I(t)$ applied to the cell (galvanostatic mode) and the output is the terminal voltage $V(t)$ measured between the positive and negative current collectors and resulting from the sum of the potential and overpotential terms according to

$$\begin{aligned} V(t) = {} & (U^{\rm p}(t) - U^{\rm n}(t)) + (\eta^{\rm p}(t) - \eta^{\rm n}(t)) \\ & + (\phi_{\rm e}^{\rm p}(L,t) - \phi_{\rm e}^{\rm n}(0,t)) - R_\Omega I(t). \end{aligned} \tag{7a}$$

The values and the meaning of the parameters appearing in this section are reported in Table VI in the Appendix.

The equilibrium potentials $U^i(t)$ depend on the lithium ion concentration at the solid-electrolyte interface $c^i_{\rm s,e}(t)$; defining the stoichiometry ratio as $\theta^i(t) = c^i_{\rm s,e}(t)/c^i_{\rm s,max} \in [0;1]$, we can write the functional form of the equilibrium potential at the cathode side as

$$\begin{aligned} U^{\rm p}(\theta^{\rm p}(t)) = {} & -10.72[\theta^{\rm p}(t)]^4 + 23.88[\theta^{\rm p}(t)]^3 \\ & - 16.77[\theta^{\rm p}(t)]^2 + 2.595\,\theta^{\rm p}(t) + 4.563 \end{aligned}$$

and at the anode side.[3] as

$$\begin{aligned} U^{\rm n}(\theta^{\rm n}(t)) = {} & 0.1493 + 0.8493\exp(-61.79\,\theta^{\rm n}(t)) \\ & + 0.3824\exp(-665.8\,\theta^{\rm n}(t)) \\ & - \exp(39.42\,\theta^{\rm n}(t) - 41.92) \\ & - 0.03131\tan^{-1}(25.59\,\theta^{\rm n}(t) - 4.099) \\ & - 0.009434\tan^{-1}(32.49\,\theta^{\rm n}(t) - 15.74). \end{aligned}$$

The kinetic overpotential terms $\eta^i(t)$ are related to the current density $j^i(t) = \mp\frac{I(t)}{A^i L^i}$ by the Butler-Volmer equation [25], whose solution is

$$\eta^i(t) = \frac{R_{\rm g}T}{\alpha F}\sinh^{-1}\left[\frac{j^i(t)}{a^i_{\rm s} i^i_0(t)}\right]. \qquad i = {\rm p,n} \tag{7b}$$

The exchange current density $i^i_0(t)$ is related to the concentration at the electrode surface and in the electrolyte, $c^i_{\rm s,e}(t)$ and $c^i_{\rm e}(t)$ respectively, through

$$i^i_0(t) = k^i\sqrt{c^i_{\rm e}(t)(c^i_{\rm s,max} - c^i_{\rm s,e}(t))c^i_{\rm s,e}(t)}. \qquad i = {\rm p,n} \tag{7c}$$

The electrolyte overpotential $\Delta\,\phi_{\rm e}(t) = \phi_{\rm e}^{\rm p}(L,t) - \phi_{\rm e}^{\rm n}(0,t)$ is computed by integrating the equation of the conservation of charge in the liquid phase under the assumption of constant current density throughout the electrodes and leads to

$$\Delta\,\phi_{\rm e}(t) = \kappa_{\rm d}(\log[c_{\rm e}^{\rm p}(t)] - \log[c_{\rm e}^{\rm n}(t)]) - I(t)R_{\rm e} \tag{7d}$$

[2]Specifications of the cell used are found in [24].

[3]Both cathode and anode overpotential equations are taken from [27]

where $\kappa_{\mathrm{d}} = \frac{2R_{\mathrm{g}}T(1-t_0^+)}{F}(1+\beta)$. The electrolyte resistance is $R_{\mathrm{e}} = \frac{1}{\kappa\varepsilon_{\mathrm{e}}}(\frac{L^{\mathrm{p}}}{A^{\mathrm{p}}} + \frac{L^{\mathrm{n}}}{A^{\mathrm{n}}})$, with the electrolyte conductivity κ that depends on temperature according to the equations detailed in [28], where the authors present a thorough experimental analysis of the electrochemical properties of a $LiPF_6$-based electrolyte.

Equations (7a) to (7d) describe the static relations between the terminal voltage, the applied current and the internal lithium concentration. The dynamic evolution of the battery voltage is due to the diffusion of the lithium concentration throughout the solid and liquid phase with current, described by the coupled PDEs of the FDN model. Many order reduction techniques are used in the literature to reduce the complexity of such equations, from finite difference methods [29] — usually characterized by a large number of states — to Galerkin orthogonal decomposition [30] and frequency-based order reduction [21], [31]. The latter are particularly appealing for control applications because of the low number of states necessary to obtain a good accuracy for standard HEV current cycles.

A state-space realization of the solid diffusion transfer function that explicitly relates the SOC to the surface concentration at the electrodes and allows to take temperature variations into account has been developed in parallel to this research and is used in this work. The overall state-space model equations are

$$\begin{aligned}
&\dot{\boldsymbol{x}}(t) = \boldsymbol{A}\boldsymbol{x}(t) + \boldsymbol{B}I(t), \quad \text{with } \boldsymbol{x} \in \mathbb{R}^7 \\
&\boldsymbol{y}(t) = \boldsymbol{C}\boldsymbol{x}(t), \qquad \text{with } \boldsymbol{y}(t) = \begin{bmatrix} \tilde{c}^{\mathrm{p}}_{\mathrm{s,e}}(t) \\ \tilde{c}^{\mathrm{n}}_{\mathrm{s,e}}(t) \\ \widetilde{SOC}(t) \\ \tilde{c}^{\mathrm{p}}_{\mathrm{e}}(t) \\ \tilde{c}^{\mathrm{n}}_{\mathrm{e}}(t) \end{bmatrix} \in \mathbb{R}^5
\end{aligned} \tag{8}$$

where $\boldsymbol{x} = [x_1, \ldots, x_7]^T$ is the vector of state variables of the battery model and the output vector $\boldsymbol{y}(t)$ comprises of the lithium concentration at the solid-electrolyte interphase of the positive and negative electrodes — i.e. at the surface of the electrode particle — ($c^{\mathrm{i}}_{\mathrm{s,e}}$, $i = \mathrm{p}, \mathrm{n}$), the cell state-of-charge and the lithium ion concentration in the electrolyte phase at the anode and cathode side ($c^{\mathrm{i}}_{\mathrm{e}}$, $i = \mathrm{p}, \mathrm{n}$). The tilde indicates a perturbation from the equilibrium conditions. The state space matrices are reported in (9), shown at the bottom of this page. Notice that the matrix $\boldsymbol{C}$ selects five out of the seven states to build the output vector $\boldsymbol{y}(t)$; the states x_2 and x_4, which are derived from a realization of a Pade's approximation-based transfer function do not appear in the output vector, but they serve to better capture the dynamics of the electrode surface concentrations over a wide range of frequencies of battery operation. The solid phase diffusion coefficients D^i_{s}, the kinetic constants k^i and the activity coefficient β become larger as temperature increases according to the Arrhenius-like equation

$$\Gamma(T) = \Gamma_{\mathrm{ref}} \exp\left[-\frac{E_{\mathrm{act},\Gamma}}{R_{\mathrm{g}}}\left(\frac{1}{T} - \frac{1}{T_{\mathrm{ref},\Gamma}}\right)\right]. \tag{10}$$

The reverse trend of R_Ω with temperature is described by the same equation (10) with a sign change inside the exponential.

F. Battery Aging

Degradation of battery performance throughout time can be traced back to many different aging mechanisms depending on electrode composition and operating conditions; comprehensive reviews can be found in [32]. It is common practice though to lump all the aging phenomena into a side irreversible reaction between the solvent and the anode material that forms a film at the solid electrolyte interface (SEI) [33], [34]. The SEI layer growth consumes cyclable Li-ions reducing the overall battery capacity and isolates the anode particles increasing its

$$\boldsymbol{A} = \begin{bmatrix}
-\frac{189D^{\mathrm{p}}_{\mathrm{s}}}{[R^{\mathrm{p}}_{\mathrm{s}}]^2} & -\frac{3465[D^{\mathrm{p}}_{\mathrm{s}}]^2}{[R^{\mathrm{p}}_{\mathrm{s}}]^4} & 0 & 0 & \frac{189D^{\mathrm{p}}_{\mathrm{s}}(\theta^{\mathrm{p}}_{100\%}-\theta^{\mathrm{p}}_{0\%})c^{\mathrm{p}}_{\mathrm{s,max}}}{[R^{\mathrm{p}}_{\mathrm{s}}]^2} & 0 & 0 \\
1 & 0 & 0 & 0 & -(\theta^{\mathrm{p}}_{100\%} - \theta^{\mathrm{p}}_{0\%})c^{\mathrm{p}}_{\mathrm{s,max}} & 0 & 0 \\
0 & 0 & -\frac{189D^{\mathrm{n}}_{\mathrm{s}}}{[R^{\mathrm{n}}_{\mathrm{s}}]^2} & -\frac{3465[D^{\mathrm{n}}_{\mathrm{s}}]^2}{[R^{\mathrm{n}}_{\mathrm{s}}]^4} & -\frac{189D^{\mathrm{n}}_{\mathrm{s}}(\theta^{\mathrm{n}}_{100\%}-\theta^{\mathrm{n}}_{0\%})c^{\mathrm{n}}_{\mathrm{s,max}}}{[R^{\mathrm{n}}_{\mathrm{s}}]^2} & 0 & 0 \\
0 & 0 & 1 & 0 & (\theta^{\mathrm{n}}_{100\%} - \theta^{\mathrm{n}}_{0\%})c^{\mathrm{n}}_{\mathrm{s,max}} & 0 & 0 \\
0 & 0 & 0 & 0 & 0 & 0 & 0 \\
0 & 0 & 0 & 0 & 0 & -\frac{9.8710D^{\mathrm{eff}}_{\mathrm{e}}}{L^2} & 0 \\
0 & 0 & 0 & 0 & 0 & 0 & -\frac{9.5842D^{\mathrm{eff}}_{\mathrm{e}}}{L^2}
\end{bmatrix}$$

$$\boldsymbol{B} = \begin{bmatrix} \frac{7}{\varepsilon^{\mathrm{p}}FA^{\mathrm{p}}L^{\mathrm{p}}} & -\frac{[R^{\mathrm{p}}_{\mathrm{s}}]^2}{15\,D^{\mathrm{p}}_{\mathrm{s}}\varepsilon^{\mathrm{p}}FA^{\mathrm{p}}L^{\mathrm{p}}} & \frac{7}{\varepsilon^{\mathrm{n}}FA^{\mathrm{n}}L^{\mathrm{n}}} & -\frac{[R^{\mathrm{n}}_{\mathrm{s}}]^2}{15\,D^{\mathrm{n}}_{\mathrm{s}}\varepsilon^{\mathrm{n}}FA^{\mathrm{n}}L^{\mathrm{n}}} & -\frac{1}{Q_{\mathrm{N}}} & \frac{3.1463(t_0^+-1)}{\varepsilon_{\mathrm{e}}LFA^{\mathrm{p}}} & -\frac{2.9351(t_0^+-1)}{\varepsilon_{\mathrm{e}}LFA^{\mathrm{n}}} \end{bmatrix}^\top$$

$$\boldsymbol{C} = \begin{bmatrix} 1 & 0 & 0 & 0 & 0 & 0 & 0 \\ 0 & 0 & -1 & 0 & 0 & 0 & 0 \\ 0 & 0 & 0 & 0 & 1 & 0 & 0 \\ 0 & 0 & 0 & 0 & 0 & 1 & 0 \\ 0 & 0 & 0 & 0 & 0 & 0 & 1 \end{bmatrix} \tag{9}$$

impedance. In this paper we borrow the reduced-order degradation model from [35], which is based on a thorough experimental campaign performed at different charge/discharge current profiles and SOC values: since the diffusion of the solvent reactants through the SEI layer is much slower than the lithium de-insertion dynamics, then the Butler-Volmer equation for the solvent reduction kinetics can be simplified as

$$j_{\mathrm{s}}(t) = -\frac{k_{\mathrm{SEI}}(T)}{2A_{\mathrm{n}}(1+\lambda\theta(t))\sqrt{t}}, \tag{11}$$

where $\theta(t) = \exp[\frac{F}{RT}(\eta^{\mathrm{n}}(t) + U^{\mathrm{n}}(t) - U_{\mathrm{sei}})]$. Notice that at higher SOC the half-cell open circuit voltage $U_{\mathrm{n}}(t)$ is small, therefore the side reaction kinetics is faster; following a similar reasoning, a cathodic current at the anode side (during charging) leads to negative surface overpotential $\eta_{\mathrm{n}}(t)$, thus accelerating the SEI formation. The fitting parameter λ weighs the effect of the anode potential on the SEI growth, while the kinetic coefficient for the side reaction $k_{\mathrm{SEI}}(T)$ follows the Arrhenius dependency reported in (10). The capacity loss associated to the SEI formation is obtained by integrating the side-reaction rate over time, namely

$$Q_{\mathrm{SEI}} = \int_0^t j_{\mathrm{s}}(t)\, A_{\mathrm{n}} \mathrm{d}t\,. \tag{12}$$

The authors of [35] claim that the increased capacity loss observed after charging and discharging cycles is due to the structural damages that constantly isolate the active material. This phenomenon is well described by the variation of the active material volume fraction that, under the uniform utilization assumption becomes

$$\frac{\mathrm{d}\varepsilon_{\mathrm{AM}}(t)}{\mathrm{d}t} = -\kappa_{\varepsilon}(T)|j_{\mathrm{n}}(t)|, \tag{13}$$

where again $\kappa_{\varepsilon}(T)$ depends on temperature according to (10). The SOC-dependent capacity loss rate induced by the volume fraction reduction is expressed as

$$\frac{\mathrm{d}Q_{\mathrm{AM}}}{\mathrm{d}t} = \frac{\mathrm{d}\varepsilon_{\mathrm{AM}}(t)}{\mathrm{d}t}\, SOC(t)\, V^{\mathrm{n}}\, c^{\mathrm{n}}_{\mathrm{s,max}}. \tag{14}$$

The total capacity loss at time $t > 0$ is modeled by assuming the superposition of the two capacity loss mechanisms, i.e.

$$\begin{aligned} Q_{\mathrm{loss}} =&\ Q_{\mathrm{SEI}} + Q_{\mathrm{AM}} \\ =&\ -\int_0^t \frac{k_{\mathrm{SEI}}(T)}{2(1+\lambda\theta(t))\sqrt{t}}\mathrm{d}t \\ &-\int_0^t \kappa_{\mathrm{AM}}(T)\, SOC(t)\, |I(t)|\mathrm{d}t, \end{aligned} \tag{15}$$

where the constant terms in (14) have been condensed in the fitting parameter $\kappa_{\mathrm{AM}}(T)$. The last term of (15) is the SOC-weighted current throughput scaled by the severity factor $\kappa_{\mathrm{AM}}(T)$. This term indicates that the aging is accelerated if the battery undergoes high charge/discharge cycles at high SOC values.

III. Battery Life-Aware Energy Management

In this section, we formulate the multi-objective optimal control problem for the battery life-aware energy management strategy and we detail the adopted solution method. Finally, we present the results of the numerical simulations and assess the effect of temperatures on the vehicle performance and on battery degradation.

A. Problem Formulation

As discussed in Section II-A, engine and motor speeds are constrained to match the velocity profile of the vehicle; this means that we can only regulate engine and motor torque (T_{eng} and T_{mot}), together with the mechanical braking torque T_{brk} and the cell current I to devise our control strategy; we define the control vector as

$$\boldsymbol{u}(t) = [T_{\mathrm{eng}}(t), T_{\mathrm{mot}}(t), T_{\mathrm{brk}}(t), I(t)]^{\top}.$$

for each t that belongs to the finite-time horizon $[0, t_{\mathrm{f}}]$, where t_{f} is the length of the selected driving cycle.

In order to take both energy savings and battery aging into account, the cost function shall include a term dependent on the capacity degradation of the battery in addition to the engine fuel consumption rate. We expect the fuel consumed (measured in liters) over the driving cycle to be much higher than the capacity loss (measured as a fraction of the initial nominal capacity). For this reason, instead of directly using these two quantities in the formulation of the objective function, we accounts for the monetary cost of fuel and battery degradation: we consider an average price of the gasoline in the European Union equal to $\Gamma_{\mathrm{fuel}} = 1.60€/liter$, while we assume that the cost of the entire 1.5 kWh battery pack is approximately equal to 900 €.[4] We assume a battery pack to be replaced when it reaches 80% of its initial capacity; indeed, after this threshold the degradation is faster and the impedance rise limits the battery power performance. This means that the total cost of the battery must be applied over a capacity loss $Q_{\mathrm{loss}} = 20\%$, resulting in a unitary cost for each percentage point of capacity loss equal to $\Gamma_{\mathrm{age}} = 45\,€/\%_{\mathrm{loss}}$.

The objective function is formulated as the weighted sum of the cost of fuel consumption over the time horizon $[0, t_{\mathrm{f}}]$ (running cost) and the cost of capacity loss at the end of the driving cycle t_{f} (terminal cost)

$$\begin{aligned} J = \alpha \int_0^{t_{\mathrm{f}}} &\Gamma_{\mathrm{fuel}}\, \dot{m}_{\mathrm{f}}(\boldsymbol{x}(t), \boldsymbol{u}(t))\, \mathrm{d}t \\ &+ (1-\alpha)\, \Gamma_{\mathrm{age}} Q_{\mathrm{loss}}\left(\boldsymbol{x}(t_{\mathrm{f}}), \boldsymbol{u}(t_{\mathrm{f}})\right), \end{aligned} \tag{16}$$

where the Pareto coefficient $0 \leq \alpha \leq 1$ weights the two terms. The capacity loss $Q_{\mathrm{loss}}(\cdot)$ is as in (15) and the instantaneous fuel consumption rate $\dot{m}_{\mathrm{f}}(\cdot)$ has been defined in (3). The states $\boldsymbol{x} \in \mathbb{R}^7$ follow the battery dynamics detailed in (8). The electrode

[4] This is the approximate cost of the battery replacement for a Toyota Prius C taken from [36] and adapted to the battery cost per kWh to 2019 pricing as reported in [37]. This value is used just to scale the battery degradation term in the cost function (16) so to have the same order of magnitude of the fuel consumption term.

surface concentrations have to remain within their maximum and minimum values, i.e. $c^i_{\mathrm{s,min}} \leq c^i_{\mathrm{s}} \leq c^i_{\mathrm{s,max}}$, $i = \mathrm{p}, \mathrm{n}$. The cell voltage (7a) should remain within the safety range indicated on the cell datasheet, namely $2.4\,V \leq V(t) \leq 4.2\,V$, for each $t \in [0, t_{\mathrm{f}}]$. The knowledge of the internal surface concentrations and the constraints on the battery terminal voltage allow to expand the limits on the battery SOC without the risk of incurring in local over-charges or over-discharges, thus guaranteeing the safety conditions; the SOC is therefore constrained to vary within $SOC_{\min} = 15\%$ and $SOC_{\max} = 95\%$. The initial battery SOC is set to $SOC(0) = 50\%$ and the charge sustaining condition, typical of the non-plugin HEV, is enforced by constraining the final battery SOC to remain within a small window around its initial value, namely $SOC(0) - \mathrm{tol} \leq SOC(t_f) \leq SOC(0) + \mathrm{tol}$, where we set $\mathrm{tol} = 2\%$.

Finally, the engine and motor torques have to guarantee the torque split condition in (1), while the battery power in (6) must equate the electric motor power requirement in (4).

B. Solution Method

The *direct* approach, based on a proper discretization of the infinite dimensional optimal control problem, is recommended in [38] for the solution of large scale problems. The resulting finite dimensional problem can be solved by nonlinear programming techniques. In this work we adopt the direct approach for the discretization of the problem described in Section III-A, then we solve the resulting finite dimensional problem with the interior-point algorithm implemented in the state-of-the-art solver Ipopt [39].

We define the equidistant grid $\mathbb{G}_N = \{t_0 < t_1 < \ldots < t_N = t_{\mathrm{f}}\}$, with constant time step $t_{\mathrm{s}} = \frac{t_N - t_0}{N}$ and grid points $t_j = t_0 + j\,t_{\mathrm{s}}, j = 1, \ldots, N$. We set $t_{\mathrm{s}} = 0.5$ s for each driving cycle, therefore the length of the discretization grid is determined by the initial and the final time instants.

We approximate the controls on the grid $\mathbb{G}_N$ with piecewise constant functions. We then discretize the differential equation (8) using the Tustin method, that yields

$$\begin{aligned} \boldsymbol{x}(t_{j+1}) = &\left[\left(\boldsymbol{I}\boldsymbol{I}_{n_x} - \frac{t_{\mathrm{s}}}{2}\boldsymbol{A}\right)^{-1}\left(\boldsymbol{I}\boldsymbol{I}_{n_x} + \frac{t_{\mathrm{s}}}{2}\boldsymbol{A}\right)\right]\boldsymbol{x}(t_j) \\ &+ \left[\left(\boldsymbol{I}\boldsymbol{I}_{n_x} - \frac{t_{\mathrm{s}}}{2}\boldsymbol{A}\right)^{-1}\boldsymbol{B}\,t_{\mathrm{s}}\right]\boldsymbol{u}\left(t_{j+\frac{1}{2}}\right), \quad j=0,\ldots,N-1 \end{aligned} \tag{17}$$

where $\boldsymbol{u}(t_{j+\frac{1}{2}}) = \frac{\boldsymbol{u}_{t_j} + \boldsymbol{u}_{t_{j+1}}}{2}$, $\boldsymbol{I}\boldsymbol{I}_{n_x}$ is the $n_x \times n_x$ identity matrix and the continuous state-space matrices $\boldsymbol{A}$ and $\boldsymbol{B}$ are as in (8). Similarly, we discretize the objective function (16) and the constraints on the grid $\mathbb{G}_N$.

Ipopt is a gradient based optimizer that requires the gradient of the objective function and the Jacobian of the constraints (and optionally the Hessian of the Lagrange function); we provide the required derivatives with the algorithmic differentiator ADiGator [40]. We solved the optimal control problem running ADiGator and Ipopt on Matlab 2017b on a 2.5 GHz Intel i5 processor with 2 cores and with 16 GB of memory.

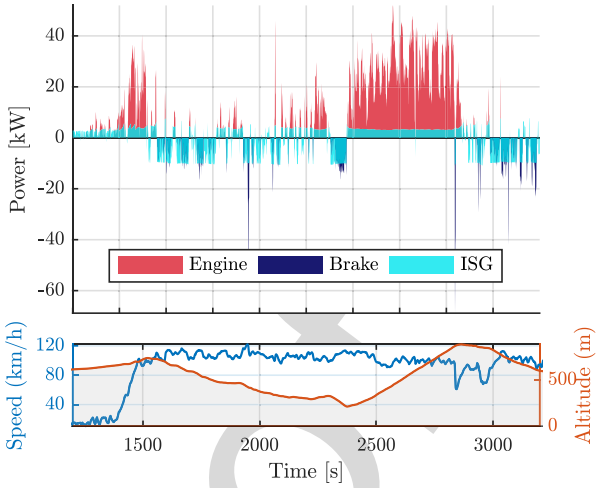

Fig. 6. Optimal power split of the hybrid transmission for the Vail2NREL cycle.

In the following section we show the results of the simulations that have been run several times with different values of the Pareto coefficient α and at different temperatures.

IV. Simulation Results

In this section we first show the solution of the energy management problem without considering the battery aging, i.e. we set $\alpha = 1$ in the cost function (16). Then, we solve the energy management problem to changing values of the Pareto coefficient; in this way we show how different weights on the two objectives — energy management and battery preserving — affect the control strategy. Finally, we repeat the optimization for changing values of the battery temperature. Despite a global optimum cannot be guaranteed due to non-convexity and non-linearity of the problem, the adoption of the Monotonic Basin Hopping approach in this paper [41] to search for the best local optimum allows to explore the space of the solutions more thoroughly by starting from different initial guesses.

A. Solution to the Energy Management Problem

The optimization has been solved for the four driving cycles presented in Section II-A, but we report in the following figures only the results of the Vail2NREL cycle.

In the first simulation scenario, we set the battery temperature to 30° C and we select the Pareto coefficient $\alpha = 1$ to find the solution that optimizes solely the fuel consumption. In Fig. 6 we present the optimal power split resulting from the solution of the optimization problem. We see that the electric machine assists the engine with an approximately constant power; this is possible because most of the braking energy is recovered by the generator and the mechanical brakes intervene only when the braking maneuver is too severe. It is also interesting to notice that the optimal control uses the energy recovered in the last part of the driving cycle to restore the battery SOC to its initial value, as imposed by the constraints defined in Section III-A and shown in Fig. 7 on a cell level. The a-priori knowledge of

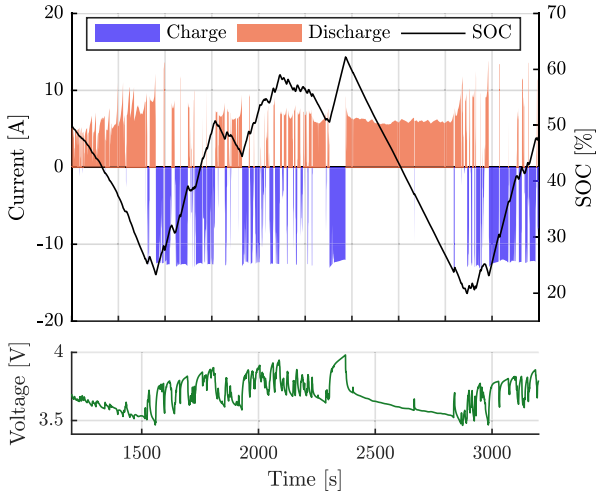

Fig. 7. Cell current, SOC and voltage profiles throughout the Vail2NREL cycle.

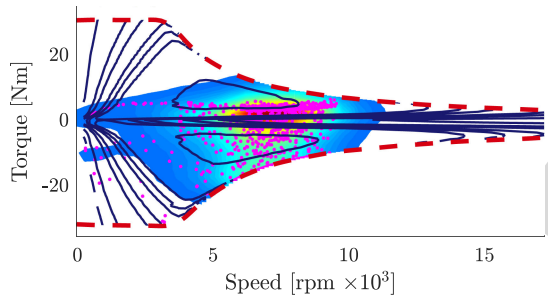

Fig. 8. Electric machine utilization throughout the Vail2NREL cycle.

the road slope in the Vail2NREL driving cycle allows for an intelligent management of the battery, recovering energy during the downhills that is used to assist the engine during the uphills. We see from Fig. 7 that neither the battery current, onr the voltage or SOC bounds are limiting the electric performance, since they lay within their admissible range throughout the driving cycle. This means that the capability of the electric system to recover or release power is restricted by the torque limits of the electric machine, as illustrated in Fig. 8.

Nevertheless, it is clear form Fig. 8 that the optimal control manages to make the ISG work in the proximity of its highest efficiency regions. This is particularly true when the electric machine is working in motor mode, while when the electric machine is regenerating, even the less efficient regions are exploited: this leads to conclude that, from the electric machine perspective, it is fundamental to recover as much energy as possible, not necessarily in an efficient way.

The fuel savings for the four driving cycles are reported in Table III. The best fuel savings performances are obtained in the WLTC cycle, since the frequent acceleration and deceleration maneuvers — and the resulting charge/discharge profiles — allow to use the battery in the most effective way; the US06 driving cycle exhibits the lowest fuel savings performance, because of the almost constant high speed for most of the cycle time that prevents the battery from re-charging.

TABLE III
FUEL SAVINGS WITH OPTIMAL ENERGY MANAGEMENT CONTROL OF THE HYBRID ELECTRIC VEHICLE

	WLTC	Vail2NREL	US06	NEDC
Only engine (l)	1.04	1.65	0.49	0.51
HEV (l)	0.88	1.45	0.44	0.44
Savings	15.4%	12.1%	10.2%	13.7%

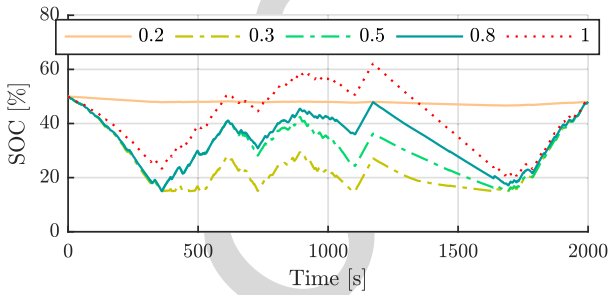

Fig. 9. Comparison of battery SOC profiles for different values of the Pareto coefficient α over the Vail2NREL cycle.

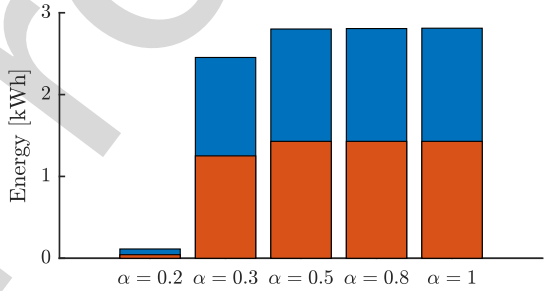

Fig. 10. Comparison of the battery energy throughput (charge in orange and discharge in blue) for different values of the Pareto coefficient α.

B. Solution to Changing Pareto Coefficient

By reducing the value of the Pareto coefficient α in (16) we give more importance to the mitigation of the capacity degradation of the battery, penalizing the fuel consumption minimization.

In Fig. 9 we show the SOC profiles at different values of the Pareto coefficient: the SOC trends look similar for $\alpha \geq 0.5$, but its average value gets smaller and smaller. For values of the Pareto coefficient close to zero the SOC remains approximately constant around its initial value, because almost no energy is delivered by the battery, nor stored into it as depicted in Fig. 10; this means that the electric branch of the hybrid powertrain is not used to preserve the heath of the battery. This is of course an unwanted behavior, because it does not bring any advantage to the fuel savings performance; to this end we must select higher values of α, in particular, for this powertrain configuration, we choose $\alpha \geq 0.5$.

We reported in Table IV the fuel savings for the four driving cycles and for different values of the Pareto coefficient. The values in Table IV represent the reduction (in percentage) of the fuel consumed over each driving cycle compared to the ICE-only architecture. As expected, almost no fuel saving improvement

TABLE IV
FUEL SAVINGS COMPARISON FOR DIFFERENT VALUES OF THE PARETO COEFFICIENT α. SAVINGS ARE REFERRED TO THE FUEL CONSUMPTION WITH ONLY ICE

(%)	WLTC	Vail2NREL	US06	NEDC
$\alpha = 0.2$	0.9	1.0	1.4	1.6
$\alpha = 0.5$	14.7	13.7	10.5	13.2
$\alpha = 0.8$	15.2	13.9	10.7	13.6
$\alpha = 1.0$	15.4	14.1	10.7	13.7

TABLE V
REDUCTION OF THE CAPACITY DEGRADATION FOR $\alpha < 1$. THE EXACT FORMULA TO COMPUTE THE PERCENTAGE VALUES IN THE TABLE IS $(1 - Q_{\text{loss}}(\alpha)/Q_{\text{loss}}(\alpha = 1)) \times 100$

(%)	WLTC	Vail2NREL	US06	NEDC
$\alpha = 0.2$	96.1	96.3	95.0	94.2
$\alpha = 0.5$	27.1	24.5	5.5	11.0
$\alpha = 0.8$	14.1	18.5	1.1	1.8
$\alpha = 1.0$	0	0	0	0

is achieved, compared to the ICE only, for values of α close to zero; meanwhile, for $\alpha \geq 0.5$ similar fuel reduction values are obtained. This result is justified by inspecting the total energy throughput of the battery in Fig. 10, that is almost identical for the solutions with $\alpha \geq 0.5$, despite the different average states of charge.

Although fuel savings remain approximately the same for values of the Pareto coefficient greater than 0.5, on the other hand a significant decrease of the battery deterioration is obtained, as shown in Table V, where the percentage reduction in capacity degradation w.r.t. the case with $\alpha = 1$ is reported. This case corresponds to solving the optimization problem (16) without the degradation cost, which in turn correspond to the worst case scenario as far as battery aging goes. For $\alpha = 0.2$ we simulate a negligible deterioration of the battery capacity, due to the battery inactivity during the driving cycle. For intermediate values of the Pareto coefficient, namely $0.5 \leq \alpha \leq 0.8$, we found a meaningful reduction of the battery deterioration. This is a remarkable result, since we can slow down battery aging without significantly affecting the fuel savings capabilities of the electric hybrid powertrain; indeed, the control strategy computed with $\alpha = 0.5$ in the WLTC driving cycle, allows to obtain almost the same fuel reduction performance while reducing the aging rate by 27%.

The motivation of these results can be found in the degradation model (15): first, lower SOC leads to higher values of the open circuit anode-potential $U_{\text{n}}(\cdot)$, slowing down the SEI layer growth; second and most important, the SOC-weighted energy throughput — *i.e.* the last term of (15) — is considerably reduced for lower values of the Pareto coefficient as shown in Fig. 11, leading to a much slower degradation associated to the charge/discharge cycles of the battery.

In the following we show how the operating temperature of the battery affects both the fuel savings performance and the battery degradation rate.

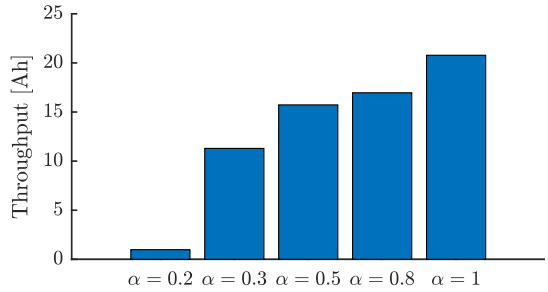

Fig. 11. Comparison of the SOC-weighted current throughput for different values of the Pareto coefficient α.

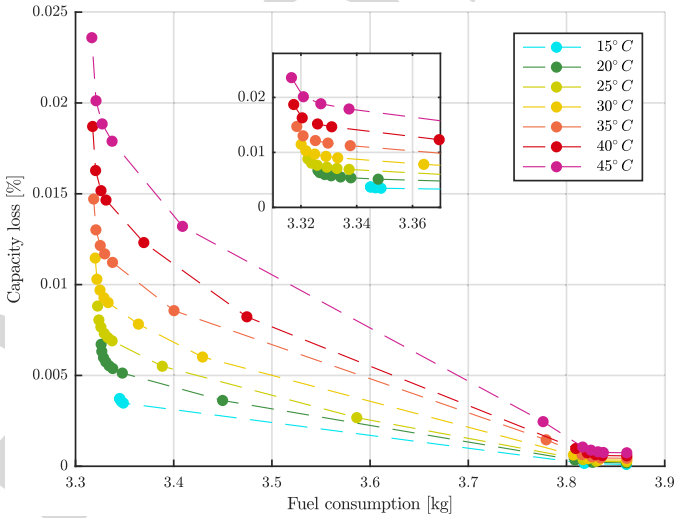

Fig. 12. Pareto curves for the four concatenated driving cycles, with the leftmost points corresponding to higher values of α.

C. Solution to Changing Temperature

We have seen in Section II-D that the temperature accelerates the kinetics of the side reactions that lead to capacity loss and impedance increase, reducing the life span of the battery pack. On the other side, too cold temperatures slow down the diffusion reactions with a consequent increase of the battery impedance, having a detrimental effect on the overall efficiency.

The cooling system of a battery pack is designed to prevent the battery temperature from reaching too high values, in order to extend the battery life and to avoid unsafe operating conditions (e.g. thermal runaway). The cooling system activates when the temperature of the battery exceeds a certain threshold, that is selected according to a compromise between performance optimization and battery life. In the following we show how such threshold, together with the selection of the Pareto coefficient, influences the optimization results.

The Pareto curves of Fig. 12 have been drawn by simulating the capacity loss and the fuel consumption for different values of the Pareto coefficient changing the temperature and concatenating the four driving cycles (WLTC, Vail2Nrel, US06 and NEDC). The Pareto coefficients being equal, there is a clear reduction of the capacity loss at lower temperatures, due to the

TABLE VI
LIST OF PARAMETERS OF THE GR/NMC 2.0AH 3.7 V CELL

Description	Unit	Symbol	Value	Source
Faraday Const.	$\frac{\mathrm{C}}{\mathrm{mol}}$	F	96487	-
Gas Const.	$\frac{\mathrm{J}}{\mathrm{mol\,K}}$	R_{g}	8.3140	-
Nom.Capacity	Ah	Q_{N}	2.0	ds
Brugg. coeff.	–	γ	1.5	[42]
Avg. liquid conc.	$\frac{\mathrm{mol}}{\mathrm{cm}^3}$	$c_{\mathrm{e,avg}}$	$1.2 \cdot 10^{-3}$	[42]
Electrode Area	cm^2	A^{p} A^{n}	$1.0204 \cdot 10^{3}$ $1.0204 \cdot 10^{3}$	[42]
Layer thickness	cm	L^{p} L^{s} L^{n}	$3.65 \cdot 10^{-3}$ $2.50 \cdot 10^{-3}$ $4.00 \cdot 10^{-3}$	[42]
Volume Fraction	-	ε^{p} ε^{s} ε^{n}	0.6395 0.3000 0.6500	id.
Max. Li conc.	$\frac{\mathrm{mol}}{\mathrm{cm}^3}$	$c^{\mathrm{p}}_{\mathrm{s,max}}$ $c^{\mathrm{n}}_{\mathrm{s,max}}$	0.0518 0.0311	[42]
Initial stoich.	-	$\theta^{\mathrm{p}}_{0\%}$ $\theta^{\mathrm{n}}_{0\%}$	0.9518 0.0168	id.
Final stoich.	-	$\theta^{\mathrm{p}}_{100\%}$ $\theta^{\mathrm{n}}_{100\%}$	0.3176 0.9664	id.
Particle Radius	cm	$R^{\mathrm{p}}_{\mathrm{s}}$ $R^{\mathrm{n}}_{\mathrm{s}}$	$5 \cdot 10^{-4}$ $5 \cdot 10^{-4}$	[42]
Active surface	cm^{-1}	$a^{\mathrm{p}}_{\mathrm{s}}$ $a^{\mathrm{n}}_{\mathrm{s}}$	$3.8373 \cdot 10^{3}$ $3.9000 \cdot 10^{3}$	[42]
Kinetic coeff.	$\frac{\mathrm{A\,cm}^{\frac{3}{2}}}{\mathrm{mol}^{\frac{3}{2}}}$	$k^{\mathrm{p}}_{\mathrm{ref}}$ $k^{\mathrm{n}}_{\mathrm{ref}}$	1 2.97	id.
- ref. temp.	K	$T^{\mathrm{p}}_{\mathrm{ref},k}$ $T^{\mathrm{n}}_{\mathrm{ref},k}$	283 296	tune
- acti. energy	$\frac{\mathrm{J}}{\mathrm{mol}}$	$E^{\mathrm{p}}_{\mathrm{act},k}$ $E^{\mathrm{n}}_{\mathrm{act},k}$	$8.4720 \cdot 10^{4}$ $3.33 \cdot 10^{5}$	id.
Diffusion coeff.	$\frac{\mathrm{cm}^2}{s}$	$D^{\mathrm{p}}_{\mathrm{s,ref}}$ $D^{\mathrm{n}}_{\mathrm{s,ref}}$	$1.314 \cdot 10^{-10}$ $1.001 \cdot 10^{-10}$	id.
- ref. temp.	K	$T^{\mathrm{p}}_{\mathrm{ref,D_s}}$ $T^{\mathrm{n}}_{\mathrm{ref,D_s}}$	296 296	tune
- act. energy	$\frac{\mathrm{J}}{\mathrm{mol}}$	$E^{\mathrm{p}}_{\mathrm{act,D_s}}$ $E^{\mathrm{n}}_{\mathrm{act,D_s}}$	$1.721 \cdot 10^{5}$ $1.123 \cdot 10^{5}$	id.
Contact res.		$R_{\Omega,\mathrm{ref}}$	$4.6 \cdot 10^{-3}$	id.
- ref. temp.	K	$T_{\mathrm{ref},R_\Omega}$	296	tune
- acti. energy	$\frac{\mathrm{J}}{\mathrm{mol}}$	$E_{\mathrm{act},R_\Omega}$	$5.67 \cdot 10^{3}$	id.
Activity coeff.		β_{ref}	2.35	tune
- ref. temp.	K	$T_{\mathrm{ref},\beta}$	338	tune
- act. energy	$\frac{\mathrm{J}}{\mathrm{mol}}$	$E_{\mathrm{act},\beta}$	$1.164 \cdot 10^{3}$	tune

Arrhenius-like equations governing the side-reaction kinetics. It is interesting to notice that in the leftmost part of the plot, i.e. for higher values of α, a small reduction of the Pareto coefficient leads to a remarkable decrease of the capacity loss together with minor changes of the fuel consumption; this is an important outcome of our work, that proves that we can use control strategies that aim at preserving the battery life without affecting the fuel savings capability of the electric hybrid powertrain.

The fuel-saving performance degradation at lower temperatures are more visible in the left-most part of the plot, where we notice a slight variation of the fuel consumption at different temperatures. For the driving cycles studied in this work, these variations are almost negligible due to the fact the the battery operates far from the imposed constraints on voltage and surface concentration; more severe cycles, or a smaller battery, could result in a greater relevance of the operating temperature on the fuel savings performance.

V. CONCLUSION

In this paper, we presented a battery health-aware energy management strategy for a parallel HEV powertrain, based on an accurate model of the vehicle powertrain and of the battery charge/discharge dynamics and aging mechanisms. We have shown that the proposed strategy can prolong the battery lifespan up to 18 % for some driving cycles, keeping the fuel savings performance substantially unaltered. We have seen that the degradation rate of the battery is slower at lower temperatures, meaning that a good cooling system is of paramount importance in preserving the battery health. Yet, the cooling system drains power from the battery, affecting the overall fuel efficiency performance; this has not been taken into account in this work and it will be the subject of future investigations. The results proposed in this study are obtained computing off-line the solution of the optimal control problem on several driving cycles and could serve as a benchmark to assess the performance of on-line control algorithms. Future development of this research will focus on the application of the presented approach in the framework of non-linear model predictive control, in order to devise on-line energy management strategies based on accurate models of the powertrain components.

APPENDIX A

The value of the electrochemical battery parameters are reported in Table VI.

REFERENCES

[1] T.-K. Lee, Y. Kim, A. Stefanopoulou, and Z. S. Filipi, "Hybrid electric vehicle supervisory control design reflecting estimated lithium-ion battery electrochemical dynamics," in *Proc. Amer. Control Conf.*, 2011, pp. 388–395.

[2] X. Zhang and Z. Filipi, "Optimal supervisory control of the series hev with consideration of temperature effects on battery fading and cooling loss," *SAE Int. J. Alternative Powertrains*, vol. 5, no. 2, pp. 299–307, 2016.

[3] B. Sampathnarayanan, S. Serrao, S. Onori, G. Rizzoni, and S. Yurkovich, "Model predictive control as an energy management strategy for series hybrid electric vehicles," in *Proc. ASME Dyn. Syst. Control Conf.*, 2009. Q3

[4] U. Sartori, F. Biral, E. Bertolazzi, and S. Onori, "On-line power management optimization of a hybrid electric vehicle with non linear MPC and battery re-charge equivalent cost," in *Proc. 42nd Annu. Conf. IEEE Ind. Electron. Soc.*, 2016, pp. 5094–5100.

[5] S. Onori, L. Serrao, and G. Rizzoni, *Hybrid Electric Vehicles, Energy Management Strategies*. Berlin, Germany: Springer, 2016. [Online]. Available: http://link.springer.com/10.1007/978-1-4471-6781-5

[6] L. Serrao, S. Onori, and G. Rizzoni, "A comparative analysis of energy management strategies for hybrid electric vehicles," *J. Dyn. Syst., Meas., Control*, vol. 133, no. 3, 2011, Art. no. 031012.

[7] C. Musardo, G. Rizzoni, Y. Guezennec, and B. Staccia, "A-ECMS: An adaptive algorithm for hybrid electric vehicle energy management," *Eur. J. Control*, vol. 11, no. 4-5, pp. 509–524, 2005.

[8] T. Nüesch, P. Elbert, M. Flankl, C. Onder, and L. Guzzella, "Convex optimization for the energy management of hybrid electric vehicles considering engine start and gearshift costs," *Energies*, vol. 7, no. 2, pp. 834–856, 2014.

[9] N. Murgovski, L. Johannesson, X. Hu, B. Egardt, and J. Sjöberg, "Convex relaxations in the optimal control of electrified vehicles," in *Proc. Amer. Control Conf.*, 2015, pp. 2292–2298.

[10] T. Liu, B. Wang, and C. Yang, "Online markov chain-based energy management for a hybrid tracked vehicle with speedy Q-learning," *Energy*, vol. 160, pp. 544–555, 2018.

[11] T. Liu, H. Xu, W. Hu, and Y. Zou, "A heuristic planning reinforcement learning-based energy management for power-split plug-in hybrid electric vehicles," *IEEE Trans. Ind. Informat.*, vol. 15, no. 12, pp. 6436–6445, Dec. 2019.

[12] T. Liu, X. Tang, H. Wang, H. Yu, and X. Hu, "Adaptive hierarchical energy management design for a plug-in hybrid electric vehicle," *IEEE Trans. Veh. Technol.*, vol. 68, no. 12, pp. 11513–11522, Dec. 2019.

[13] X. Hu, T. Liu, X. Qi, and M. Barth, "Reinforcement learning for hybrid and plug-in hybrid electric vehicle energy management," *IEEE Ind. Electron. Mag.*, vol. 13, no. 3, pp. 16–25, Sep. 2019.

[14] L. Serrao, S. Onori, A. Sciarretta, Y. Guezennec, and G. Rizzoni, "Optimal energy management of hybrid electric vehicles including battery aging," in *Proc. Amer. Control Conf.*, 2011, pp. 2125–2130.

[15] L. Tang, G. Rizzoni, and S. Onori, "Energy management strategy for HEVs including battery life optimization," *IEEE Trans. Transp. Electrific.*, vol. 1, no. 3, pp. 211–222, Oct. 2015.

[16] S. J. Moura, J. L. Stein, and H. K. Fathy, "Battery-health conscious power management in plug-in hybrid electric vehicles via electrochemical modeling and stochastic control," *IEEE Trans. Control Syst. Technol.*, vol. 21, no. 3, pp. 679–694, May 2013.

[17] X. Hu, C. M. Martinez, and Y. Yang, "Charging, power management, and battery degradation mitigation in plug-in hybrid electric vehicles: A unified cost-optimal approach," *Mech. Syst. Signal Process.*, vol. 87, pp. 4–16, 2017.

[18] T. M. Padovani, M. Debert, G. Colin, and Y. Chamaillard, "Optimal energy management strategy including battery health through thermal management for hybrid vehicles," in *Proc. Adv. Automotive Control*, 2013, pp. 384–389.

[19] X. Hu, S. Li, and H. Peng, "A comparative study of equivalent circuit models for li-ion batteries," *J. Power Sources*, vol. 198, pp. 359–367, 2012.

[20] K. A. Smith, "Electrochemical modeling, estimation and control of lithium ion batteries," 2006.

[21] K. A. Smith, "Electrochemical control of lithium-ion batteries," *IEEE Control Syst.*, vol. 30, no. 2, pp. 18–25, Apr. 2010.

[22] A. Marotta, J. Pavlovic, B. Ciuffo, S. Serra, and G. Fontaras, "Gaseous emissions from light-duty vehicles: moving from nedc to the new wltp test procedure," *Environ. Sci. Technol.*, vol. 49, no. 14, pp. 8315–8322, 2015.

[23] G. Paganelli, G. Ercole, A. Brahma, Y. Guezennec, and G. Rizzoni, "General supervisory control policy for the energy optimization of charge-sustaining hybrid electric vehicles," *JSAE Rev.*, vol. 22, no. 4, pp. 511–518, 2001.

[24] A. Allam and S. Onori, "An interconnected observer for concurrent estimation of bulk and surface concentration in the cathode and anode of a lithium-ion battery," *IEEE Trans. Ind. Electronics*, vol. 65, no. 9, pp. 7311–7321, Sep. 2018.

[25] J. Newman and K. E. Thomas-Alyea, *Electrochemical Systems*. Hoboken, NJ, USA: Wiley, 2012.

[26] R. Klein, N. A. Chaturvedi, J. Christensen, J. Ahmed, R. Findeisen, and A. Kojic, "Electrochemical model based observer design for a lithium-ion battery," *IEEE Trans. Control Syst. Technol.*, vol. 21, no. 2, pp. 289–301, Mar. 2012.

[27] T. R. Tanim, C. D. Rahn, and C.-Y. Wang, "A temperature dependent, single particle, lithium ion cell model including electrolyte diffusion," *J. Dyn. Syst., Meas., Control*, vol. 137, no. 1, 2015, Art. no. 011005.

[28] L. O. Valøen and J. N. Reimers, "Transport properties of $lipf_6$-based li-ion battery electrolytes," *J. Electrochem. Soc.*, vol. 152, no. 5, pp. A882–A891, 2005.

[29] M. Corno, N. Bhatt, S. M. Savaresi, and M. Verhaegen, "Electrochemical model-based state of charge estimation for Li-ion cells," *IEEE Trans. Control Syst. Technol.*, vol. 23, no. 1, pp. 117–127, 2015.

[30] L. Cai and R. E. White, "An efficient electrochemical–thermal model for a lithium-ion cell by using the proper orthogonal decomposition method," *J. Electrochem. Soc.*, vol. 157, no. 11, pp. A1188–A1195, Jan. 2010.

[31] J. C. Forman, S. Bashash, J. Stein, and H. Fathy, "Reduction of an electrochemistry-based Li-ion battery health degradation model via constraint linearization and padé approximation," in *Proc. Dyn. Syst. Control Conf.*, 2010, pp. 173–183.

[32] K. B. Hatzell, A. Sharma, and H. K. Fathy, "A survey of long-term health modeling, estimation, and control of lithium-ion batteries: Challenges and opportunities," in *Proc. Amer. Control Conf.*, 2012, pp. 584–591.

[33] T. R. Tanim and C. D. Rahn, "Aging formula for lithium ion batteries with solid electrolyte interphase layer growth," *J. Power Sources*, vol. 294, pp. 239–247, 2015.

[34] M. Safari, M. Morcrette, A. Teyssot, and C. Delacourt, "Multimodal physics-based aging model for life prediction of li-ion batteries," *J. Electrochem. Soc.*, vol. 156, no. 3, pp. A145–A153, 2009.

[35] X. Jin *et al.* "Physically-based reduced-order capacity loss model for graphite anodes in Li-ion battery cells," *J. Power Sources*, vol. 342, pp. 750–761, 2017.

[36] J. Voelcker, "Toyota hybrid battery replacement cost guide (2016 update)," *Green Car Rep.*, 2016.

[37] C. Martin, "Better batteries," *Bloomberg Database*, 2019.

[38] M. Gerdts, *Optimal Control of ODEs and DAEs*. Berlin, Germany: Walter de Gruyter, 2012.

[39] A. Wächter and L. T. Biegler, "On the implementation of an interior-point filter line-search algorithm for large-scale nonlinear programming," *Math. Program.*, vol. 106, no. 1, pp. 25–57, 2006.

[40] M. J. Weinstein, M. A. Patterson, and A. V. Rao, "Utilizing the algorithmic differentiation package adigator for solving optimal control problems using direct collocation," in *Proc. AIAA Guid., Navigation, Control Conf.*, 2015, Art. no. 1085.

[41] R. H. Leary, "Global optimization on funneling landscapes," *J. Global Optim.*, vol. 18, no. 4, pp. 367–383, 2000.

[42] T. R. Tanim, C. D. Rahn, and C.-Y. Wang, "State of charge estimation of a lithium ion cell based on a temperature dependent and electrolyte enhanced single particle model," *Energy*, vol. 80, pp. 731–739, 2015.

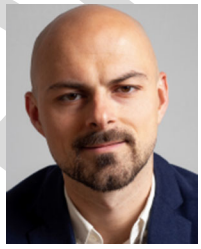

Luca De Pascali received the Ph.D. degree in mechatronics engineering, in 2019 from the University of Trento, Italy with a thesis on modelling, optimization and control of hybrid powertrains. During his studies he has been Visiting Student at Technische Universita Muünchen (Germany) and Visiting Scholar at Clemson University—International Center for Automotive Research, USA. He is currently working for Dana Incorporated on the development of electric and electric-hybrid powertrain systems for off-highway vehicles.

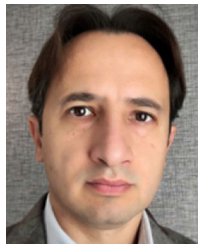

Francesco Biral received the master's degree in mechanical engineering from the University of Padova, Italy, and the Ph.D. degree in mechanism and machine theory from the University of Brescia, Italy, in 2000. He is currently Associate Professor with the Department of Industrial Engineering at University of Trento. His research interests include symbolic and numerical multi-body dynamics and optimization, constrained optimal control, mainly in the field of vehicle dynamics with special focus on intelligent vehicles.

Simona Onori (Senior Member, IEEE) received the Laurea degree, *summa cum laude*, (CSE) from the University of Rome "Tor Vergata", in 2003, the M.S. (ECE) degree from the University of New Mexico, Albuquerque, USA, in 2004, and the Ph.D. (Control Engineering) degree from the University of Rome "Tor Vergata", in 2007. She is an Assistant Professor in the Energy Resources Engineering Department at Stanford University. Her research activities are in the area of sustainable energy, for both transportation and utility sectors. She serves as the Editor-in-Chief of the *SAE International Journal of Electrified Vehicles* since 2020 and she is Distinguished Lecturer of the IEEE Vehicular Technology Society. She is the recipient of the 2019 Board of Trustees Award for Excellence, Clemson University, 2018 Global Innovation Contest Award, LG Chem, 2018 SAE Ralph R. Teetor Educational Award, 2017 NSF CAREER award. In 2020, she was elected Editor-in-Chief of the *SAE International Journal of Electrified Vehicles* and Distinguished Lecturer of the IEEE Vehicle Technology Society.